ORIGINAL ARTICLE

Surface deformation monitoring of Shanghai based on ENVISAT ASAR and Sentinel-1A data

Guohui Yao[1,2] · Chang-Qing Ke[1,3,4] · Jinhua Zhang[1,5] · Yanyan Lu[1,2] · Jiaman Zhao[1,2] · Hoonyol Lee[6]

Abstract

During urbanization, different dimensions of the expansion of construction land causes different degrees of surface deformation. Based on the C-band ENVISAT ASAR data (December 2004 to September 2010) and Sentinel-1A data (March 2015 to April 2017), the small baseline subset interferometric synthetic aperture radar (SBAS InSAR) method was used to monitor the spatial and temporal variations of surface deformation in Shanghai, China. The results showed that widespread uneven subsidence occurred in Shanghai from December 2004 to April 2017. A transition from urban areas toward the suburbs appeared in the spatial distribution, in which the cumulative deformation in the urban areas has the characteristics of seasonal fluctuation, which shows the alternation of subsidence and rebound. In addition, the deformation characteristics of different types of construction land with the same geological conditions were compared, which showed that residential land had the least cumulative subsidence and clear seasonal fluctuations, industrial land had the greatest cumulative subsidence, and transportation land had greater subsidence during the construction period but tended to become stable after being put into use. This suggests that the deformation characteristics of Shanghai are changing, and the type of construction land is also an important factor in the deformation process.

Keywords Land surface deformation · Spatial and temporal variations · Types of construction land · SBAS InSAR · Shanghai

Introduction

Surface deformation monitoring has been performed for a long time, and the techniques have been gradually promoted from the traditional leveling, global positioning system (GPS) to present synthetic aperture radar interferometry. Differential interferometric SAR (D-InSAR) incorporated the advantages of InSAR monitoring over wide areas and also improved the measurement accuracy to the millimeter scale (Massonnet et al. 1993; Wright and Stow 1999; Fruneau and Sarti 2000; Mouélic et al. 2002). Gabriel et al. (1989) were the first to use differential interferograms to observe the surface swelling characteristics of Imperial Valley in California, United States, that were caused by soil absorption properties. With the accumulation of radar observation data and further developments in data processing technology, multi-temporal InSAR techniques emerged that are able to obtain more information about the spatial and temporal variations of surface deformation while eliminating the random decorrelation errors in SAR images. The widely applied and mature algorithms of D-InSAR include

✉ Chang-Qing Ke
  kecq@nju.edu.cn

1   School of Geography and Oceanography, Nanjing University, Nanjing 210023, China

2   Jiangsu Provincial Key Laboratory of Geographic Information Science and Technology, Nanjing University, Nanjing 210023, China

3   Key Laboratory for Satellite Mapping Technology and Applications of State Administration of Surveying, Mapping and Geoinformation of China, Nanjing University, Nanjing 210023, China

4   Collaborative Innovation Center of Novel Software Technology and Industrialization, Nanjing University, Nanjing 210023, China

5   Shanghai Institute of Geological Survey, Shanghai 200072, China

6   Division of Geology and Geophysics, Kangwon National University, Chuncheon, Kangwon-do 24341, Republic of Korea

permanent scatterer interferometric synthetic aperture radar (PS InSAR) and small baseline subset interferometric synthetic aperture radar (SBAS InSAR).

The PS InSAR is mainly characterized by the extraction of pixels with relatively stable backscatter characteristics from a series of interferograms, which eliminates the influence of atmospheric disturbances on the beam signal. The deformation process of the observation period is acquired through phase spatial correlation, and then the long time series deformation is further obtained (Zebker and Villasenor 1992; Gatelli et al. 1994; Zebker et al. 1997; Hooper et al. 2004). The SBAS InSAR algorithm generates numerous interferograms of the SAR images in the same study area at different periods by setting spatial and temporal baselines and then performs singular value decomposition on all of the interferograms to obtain the deformation results of long time series (Berardino et al. 2002; Guzzetti et al. 2009). The core idea of the SBAS algorithm is to minimize the geometric decorrelation of the interferograms through small baselines (Zebker and Villasenor 1992; Hooper 2008). The SBAS algorithm has a higher temporal sampling rate than the PS algorithm, which is conducive to obtaining a deformation map with greater density that may provide a better understanding of the spatial distribution of the deformation (Berardino et al. 2002; Nikos et al. 2016).

Strozzi and Wegmuller (1999) began research on urban surface subsidence monitoring by analyzing and verifying the surface subsidence phenomenon in the urban areas of Mexico City. The internal cause of subsidence is mainly geological and geomorphological conditions and other natural factors, such as fault zone and faults (Jo et al. 2010; Cigna et al. 2012). However, in cases in which the internal mechanism is dominant, deformation occurs within short periods, such as during earthquakes (Guzzetti et al. 2009; Ogushi et al. 2015). In most cases, external mechanisms are also required, which are mainly impacts due to human activities, such as the excessive extraction of groundwater (Mouélic et al. 2002; Parcharidis et al. 2006; Chen et al. 2011; Dang et al. 2014; Pratesi et al. 2016), expansion of construction land (Dang et al. 2014; Pratesi et al. 2016), and the destruction of the bedrock by infrastructure projects (Sillerico et al. 2015). Of these factors, the excessive extraction of groundwater leads to a decrease of underground water level and an increase in soil compressibility, which causes compaction (Cabral-Cano et al. 2008); in addition, during the course of urbanization, different building structures can lead to uneven subsidence (Pratesi et al. 2016). In contrast, although the mechanism of surface subsidence is elastic (Mouélic et al. 2002), its damage to cities is irreversible: historical sites are destroyed (Tapete et al. 2012; Lubitz et al. 2013), urban underground transportation is hindered, and the efficiency of infrastructure such as bridges is reduced (Gheorghe and Armaş 2016). The destruction of flood control dams by

surface subsidence is a potential hazard to coastal cities that cannot be ignored. Surface deformation monitoring of urban areas can both provide an understanding of the order of magnitude of the deformation that has already occurred and effectively prevent geological disasters and damage to infrastructure caused by deformation by showing its spatial distribution.

As the only one megacity of urban agglomeration in the Yangtze River Delta, Shanghai began surface subsidence monitoring as early as the 1920s and has always been mainly concerned with the relationship between the excessive exploitation of groundwater and surface subsidence (Chen et al. 2013). Several scholars have tried to analyze surface subsidence from geophysical and geological perspectives. These studies found that the crust in the Yangtze River Delta was stable and that the surface subsidence was dominated by groundwater exploitation (Xiong and Zhu 2007). With the acceleration in urbanization, several scholars proposed that surface subsidence caused by engineering construction accounted for 30% of the total subsidence during the same period and that the building height and density need to be strictly controlled (Zhang et al. 2003). In recent years, many studies have examined the effects of subway tunnel excavation (Wang et al. 2011; Perissin et al. 2012; Ge et al. 2014), transportation hubs (Dong et al. 2014; Wu and Hu 2015), coastal reclamation areas (Yang et al. 2013a, b; Pepe et al. 2015, 2016; Zhao et al. 2015), and other large-scale projects on surface subsidence; although these studies involved a variety of fields, the time spans and spatial areas were very small.

In view of previous research that has shown that the SBAS algorithm can obtain denser coherent points in urban areas than the PS algorithm (Yan et al. 2012; Lauknes et al. 2008) and that C-band data have an advantage in terms of maintaining coherence (Pepe et al. 2016). C-band ENVISAT ASAR and Sentinel-1A data were used to perform analyses of the spatial–temporal distribution of surface subsidence in Shanghai using the multi-temporal SBAS InSAR method and of the deformation characteristics of different type of construction land.

Data and methods

SAR data

As the satellite that succeeded the RS-1/2, the ENVISAT ASAR satellite has higher consistency in the image mode and beam mode, and better swath width, incidence angle, and polarization and operating mode. The center frequency is 5.331 GHz, the incidence angle ranges from $-15°$ to $-45°$, and the revisit period is 35 days. 42 scenes with image mode precision (IMP) mode and HH polarization

from December 2004 to September 2010 were used, and the pixel resolution is 30*30 m (azimuth*range) (Table 1). The coverage range was approximately 56–100*100 km^2 (Fig. 1; Table 1).

Sentinel-1A is the new C-band SAR sensor that is operated by the European Space Agency (ESA). It was launched in April 2014 and has a center frequency of 5.405 GHz, incidence angle ranging from 29.1° to 46°, and a revisit period of 12 days. The sensor also supports multiple polarization combinations and imaging modes. 23 scenes with the interferometric wide swath (IW) mode and VV polarization from March 2015 to April 2017 were used, the pixel resolution is up to 5*20 m (azimuth*range), and the coverage range is up to 250 km^2 (Table 2; Fig. 1). The special swath makes the data particularly suitable for large-scale subsidence monitoring (Sowter et al. 2016).

DEM data

The Shuttle Radar Topographic Mission (SRTM) from NASA has provided digital elevation data (DEMs) for over 80% of the globe (Zyl 2001). It is currently the most widely applied global public DEM (Sun et al. 2003). The absolute vertical height accuracy (90% linear error) is 16 m and the absolute horizontal accuracy (90% circular error) is 20 m (http://www.jpl.nasa.gov/srtm/datafinaldescriptions.html), and it was resampled as a spatial resolution of approximate 90 m in China. The latest version (V4.1) of the data was used in this research to remove the topographic contribution from interferometric phase.

Leveling data

Eighteen groups of leveling point data were collected and processed as the deformation rate to determine the authenticity and accuracy of the InSAR monitoring results (Fig. 1). These leveling points are buried at depths of 1–3.3 meters. Using bedrock as the elevation point, the deformation value calculated from the latest elevation minus the previous one, unit mm.

Optical remote sensing image

Several optical images in Shanghai in May 2017 were selected from Google Earth to show the spatial distribution of the different construction land type, and the distribution map of deformation rate was rendered according to the pixel value and overlaid in ArcGIS to further analyze the surface deformation characteristics.

Table 1 ENVISAT ASAR data for the study area (Track 497 ascending pass, Swath I2)

No.	Acq. date	$B\perp$ (m)	B_{temp} (days)	No.	Acq. date	$B\perp$ (m)	B_{temp} (days)
0	13/12/2004	636	− 1540	21	04/08/2008	126	− 210
1	21/02/2005	693	− 1470	22	08/09/2008	444	− 175
2	06/06/2005	400	− 1365	23	13/10/2008	− 129	− 140
3	11/07/2005	− 575	− 1330	24	17/11/2008	300	− 105
4	19/09/2005	− 852	− 1260	25	22/12/2008	− 55	− 70
5	24/10/2005	− 532	− 1225	26	26/01/2009	331	− 35
6	13/03/2006	660	− 1085	**27**	**02/03/2009**	**0**	**0**
7	04/09/2006	108	− 910	28	06/04/2009	296	35
8	26/02/2007	− 81	− 735	29	11/05/2009	− 170	70
9	02/04/2007	467	− 700	30	20/07/2009	10	140
10	07/05/2007	− 104	− 665	31	24/08/2009	256	175
11	11/06/2007	− 52	− 630	32	28/09/2009	263	210
12	16/07/2007	126	− 595	33	02/11/2009	22	245
13	29/10/2007	158	− 490	34	07/12/2009	340	280
14	03/12/2007	222	− 455	35	11/01/2010	− 98	315
15	07/01/2008	97	− 420	36	15/02/2010	320	350
16	11/02/2008	408	− 385	37	26/04/2010	335	420
17	17/03/2008	197	− 350	38	31/05/2010	146	455
18	21/04/2008	392	− 315	39	05/07/2010	164	490
19	26/05/2008	102	− 280	40	09/08/2010	− 55	525
20	30/06/2008	− 14	− 245	41	13/09/2010	310	560

The bold values given in Table 1 and 2 are the super master image in the SBAS process. The remaining images need to be combined with it to get multiple differential interferograms. They also correspond to the 2 yellow dots in Fig. 3
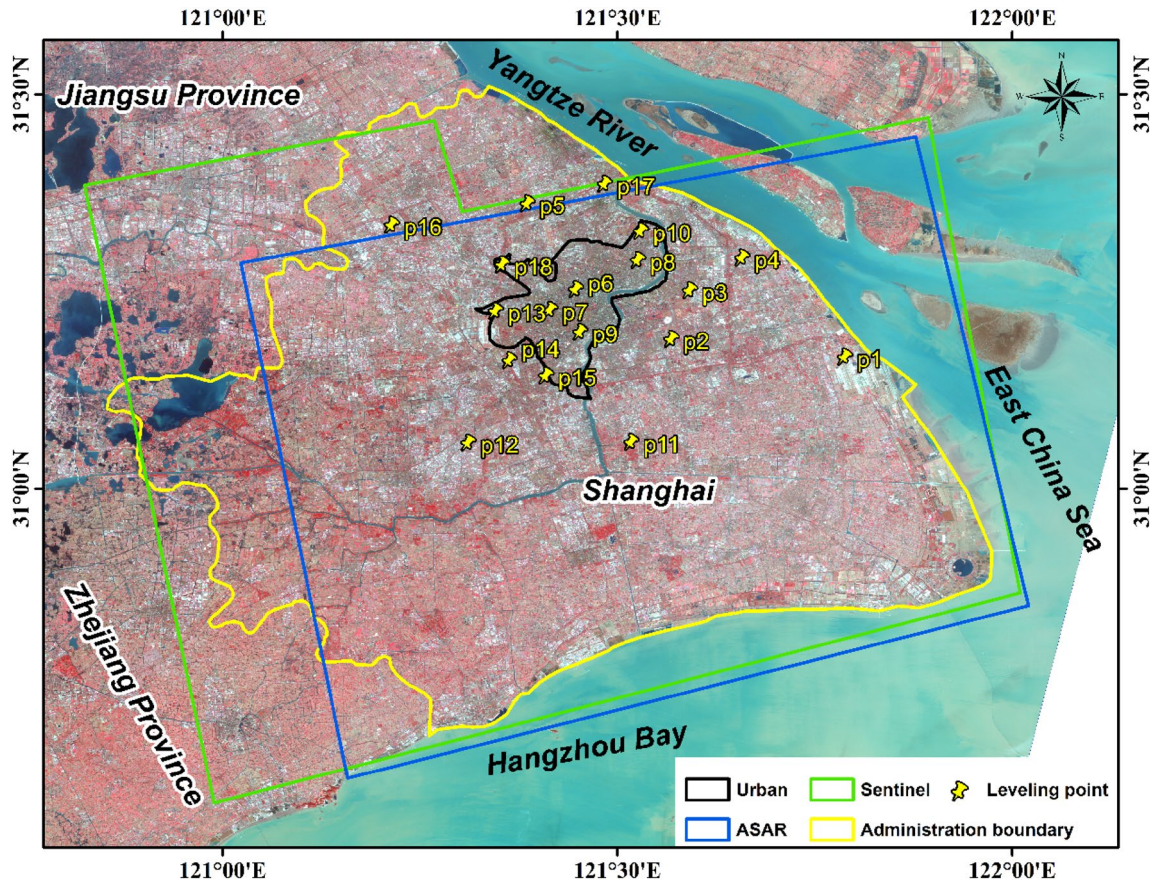
Fig. 1 Location of Shanghai, China. The background images come from Gaofen-1 (GF-1) satellite of China National Space Administration, with false color composite (R: band 4, G: band 3, B: band 2). The blue and green rectangles represent the spatial coverage of ENVISAT ASAR and Sentinel-1A, respectively, and the yellow thumbtacks represent the distribution of the 18 leveling points, which will be introduced in this section (the following third paragraph) and analyzed in the "Discussion" section

Method

The principle of the SBAS algorithm is briefly summarized as follows (Berardino et al. 2002; Guzzetti et al. 2009):

$$\delta\phi_{A-B} = \delta\phi_{def} + \delta\phi_{orb} + \delta\phi_{topo} + \delta\phi_{atm} + \delta\phi_{noise}. \quad (1)$$

Formula (1) is a common formula in interferometry that represents the composition of the phase differences in the interference image pairs, where $\delta\phi_{def}$, $\delta\phi_{orb}$, $\delta\phi_{topo}$, $\delta\phi_{atm}$, $\delta\phi_{noise}$ represent the phase difference caused by the deformation, orbital errors, topography, atmospheric disturbance, random errors, respectively. The SBAS combines a series of SAR image stacks into different sets to increase the target recognition rate by setting the lengths of the temporal and spatial baselines and removes the atmospheric phase error using the characteristics of the atmospheric disturbances, where there is a spatial correlation but no temporal correlation.

The SBAS processing flow included three parts (Fig. 2). First, a connection chart was generated by setting the temporal and spatial baselines, which could accurately represent the temporal and spatial relationships between the images (Fig. 3). Based on the connection chart, each single look complex (SLC) image is co-registered with the master image, and an interferogram was generated. These interferograms were then processed, including flattening, filtering, and coherence generation (red dashed box). The DEM data were added to refine the results, and relatively stable ground control points (GCPs) were manually selected to assist the orbital correction and absolute calibration. The surface deformation inversion could then be performed. Topographic errors and atmospheric disturbance errors were sequentially removed through two inversions (green dashed box), and the deformation rate map and the long time series deformation map were obtained though geocoding (blue dashed box).

Because the deformation in the line-of-sight (LOS) direction is affected by several factors (Lubitz et al. 2013), it was transformed into the vertical direction (VD) deformation to reduce the errors.

Table 2 Sentinel-1A data for the study area (Path 171 ascending pass, Frame 96)

No.	Acq. date	$B\perp$ (m)	B_{temp} (days)	No.	Acq. date	$B\perp$ (m)	B_{temp} (days)
0	22/03/2015	− 34	− 396	16	26/07/2016	− 66	96
1	15/04/2015	39	− 372	17	19/08/2016	− 17	120
2	09/05/2015	− 73	− 348	18	12/09/2016	− 68	144
3	08/07/2015	30	− 288	19	06/10/2016	− 38	168
4	01/08/2015	− 23	− 264	20	18/10/2016	27	180
5	25/08/2015	− 104	− 240	21	30/10/2016	15	192
6	18/09/2015	− 43	− 216	22	11/11/2016	− 34	204
7	29/11/2015	− 46	− 144	23	23/11/2016	− 74	216
8	23/12/2015	66	− 120	24	05/12/2016	− 83	228
9	16/01/2016	− 52	− 96	25	17/12/2016	− 45	240
10	09/02/2016	36	− 72	26	22/01/2017	− 24	276
11	04/03/2016	− 81	− 48	27	03/02/2017	− 40	288
12	28/03/2016	− 94	− 24	28	27/02/2017	26	312
13	**21/04/2016**	**0**	**0**	39	11/03/2017	4	324
14	15/05/2016	− 84	24	30	04/04/2017	− 72	348
15	08/06/2016	− 25	48	31	16/04/2017	− 118	360

The bold values given in Table 1 and 2 are the super master image in the SBAS process. The remaining images need to be combined with it to get multiple differential interferograms. They also correspond to the 2 yellow dots in Fig. 3

Fig. 2 Diagram of the algorithm with small baseline subset (SBAS) technology
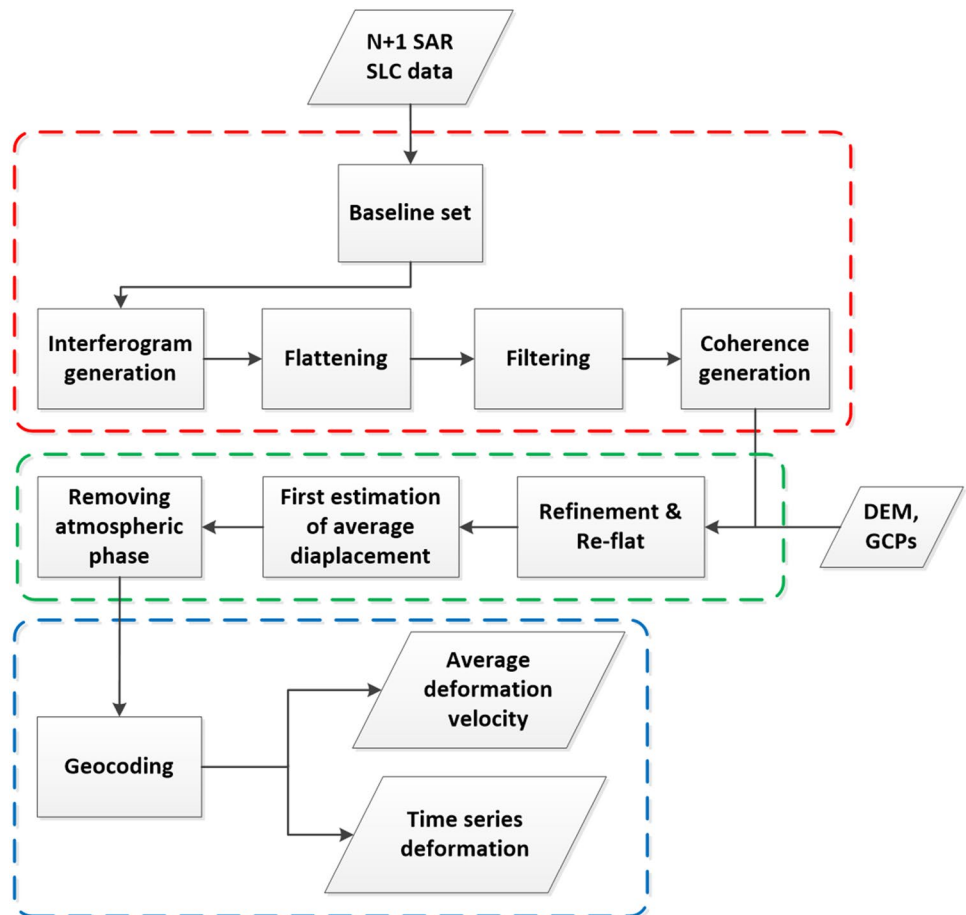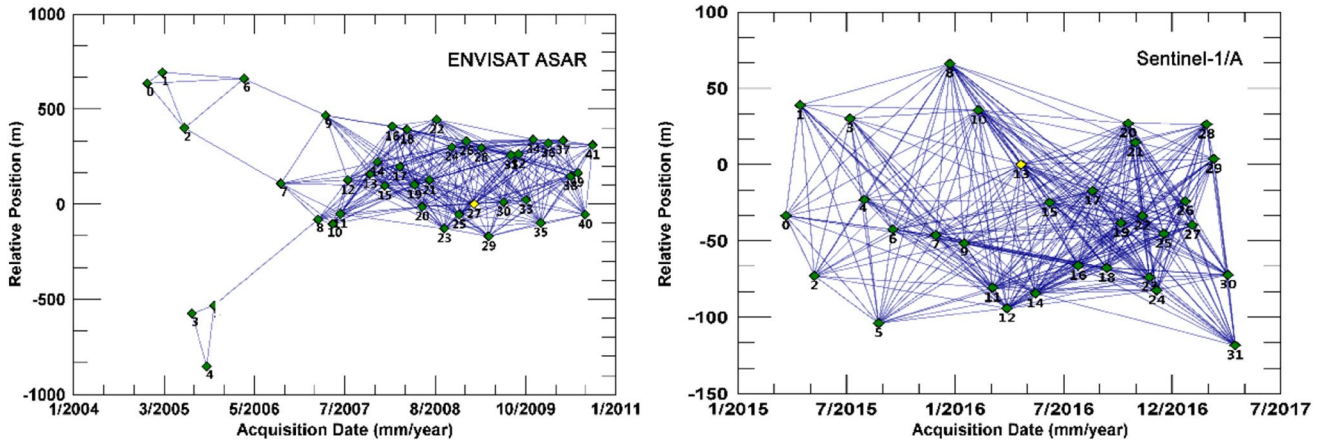
Fig. 3 Distribution of the available ENVISAT ASAR and Sentinel-1A SAR data in the temporal/perpendicular baseline domain; SAR data are represented by green diamonds and the yellow diamonds represent the super master image. Each blue line represents interferogram used in this study

Results

Spatial distribution of deformation

The ASAR results showed that the spatial distribution of the surface deformation from December 2004 to September 2010 was relatively dispersed and that there were no large areas of subsidence and rebound deformation. A nearly closed ring of subsidence was formed at the junction of Jiading, Qingpu, Songjiang, Minhang, and Changning with an average deformation rate of up to − 12 mm/year, a maximum deformation rate exceeding − 30 mm/year, and an average cumulative deformation of approximately − 50 mm (Fig. 4a). Relatively little deformation occurred within the urban areas; a subsidence zone with
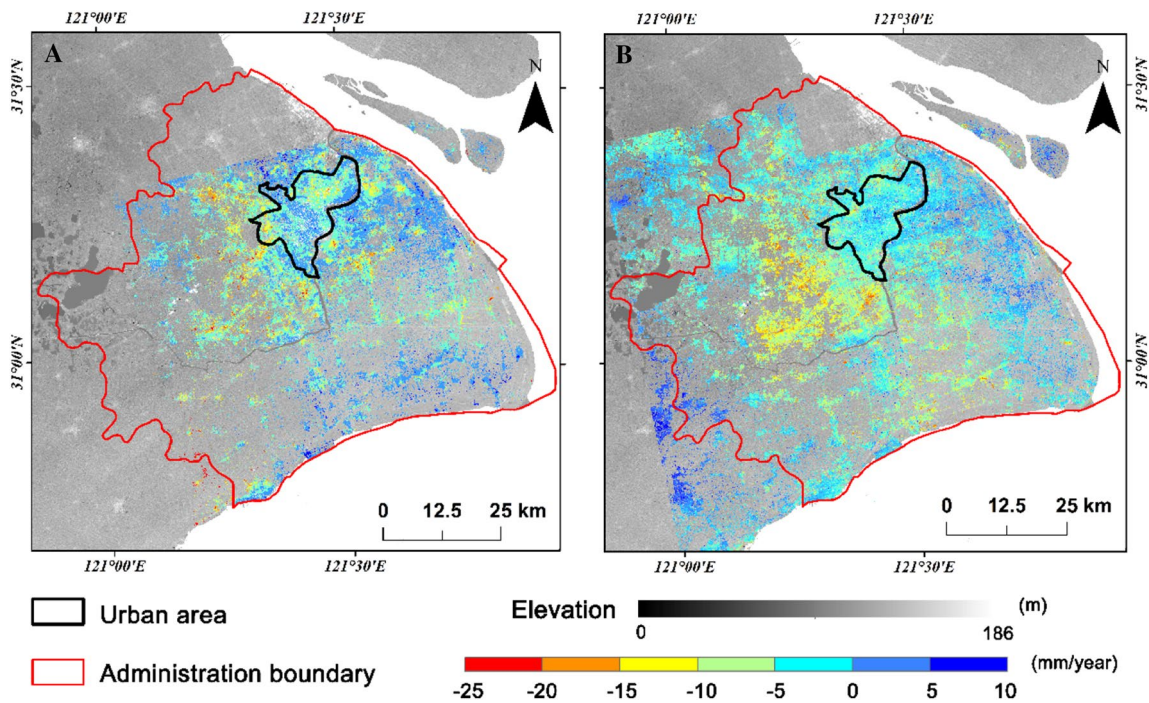
Fig. 4 Deformation rate measured by **a** ASAR from December 2004 to September 2010, **b** Sentinel-1A from March 2015 to April 2017. The background image is the SRTM DEM data

a rate of approximately − 16 mm/year was located at the border between the Yangpu District and Hongkou District. Several subsidence points were scattered in the Pudong New District and the eastern part of the Songjiang District with deformation rates between − 8 mm/year and − 19 mm/year, and linear subsidence occurred along routes S20 and S122 in the western part of the Pudong New District. A significant point-like subsidence area that reached − 13 mm/year was located at the interchange between Chengshan Road and Dongming Road. These results were consistent with the results of Lin et al. (2011), Yang et al. (2013a, b), and Chen et al. (2013).

The Sentinel-1A results showed that the surface deformation from March 2015 to April 2017 occurred in a band running from the northwest to the southeast through Jiading, Qingpu, Songjiang, Minhang, and Fengxian, with deformation rates varying from − 5 mm/year to − 20 mm/year, and the maximum deformation rate in Minhang district (Fig. 4b). The urban areas mainly rebounded; Huangpu and the southern part of Jingan rebounded the most with rates of approximately 6 mm/year and cumulative deformations of less than 3 mm. Some new subsidence occurred in the suburbs; in particular, Fengxian had a relatively large area of sparsely distributed point-like subsidence with deformation rates of approximately − 12 mm/year to − 28 mm/year and cumulative deformation varying from − 22 mm to − 43 mm.

Temporal behavior and seasonal variations

Nine test points were selected in urban areas with no factories and no excessive groundwater use or other human-caused groundwater changes to further explore the seasonal characteristics of the surface deformation (Fig. 5). Considering that the surface deformation occurred slowly with a certain lag, using 2 years as a unit, cumulative deformation curves were obtained for 2007–2008, 2009–2010, and 2015–2016. The results showed that sustained subsidence occurred from January to July of each year, and the maximum subsidence was reached around July. Afterwards, a small rebound occurred. The rebound reached a maximum around January of the second year, and a new period of subsidence accumulation began. The seasonal characteristics in 2015–2016 were the most obvious; because the amount of rebound in 2007–2008 was small, the subsidence in 2008 increased further than what had occurred in 2007.

Discussion

Comparison with leveling data

Data collected from the 10th to 18th leveling points can not be used to verify the deformation measured by ENVISAT ASAR data, for the starting time of measurement in this points was too late. The perennial deformation
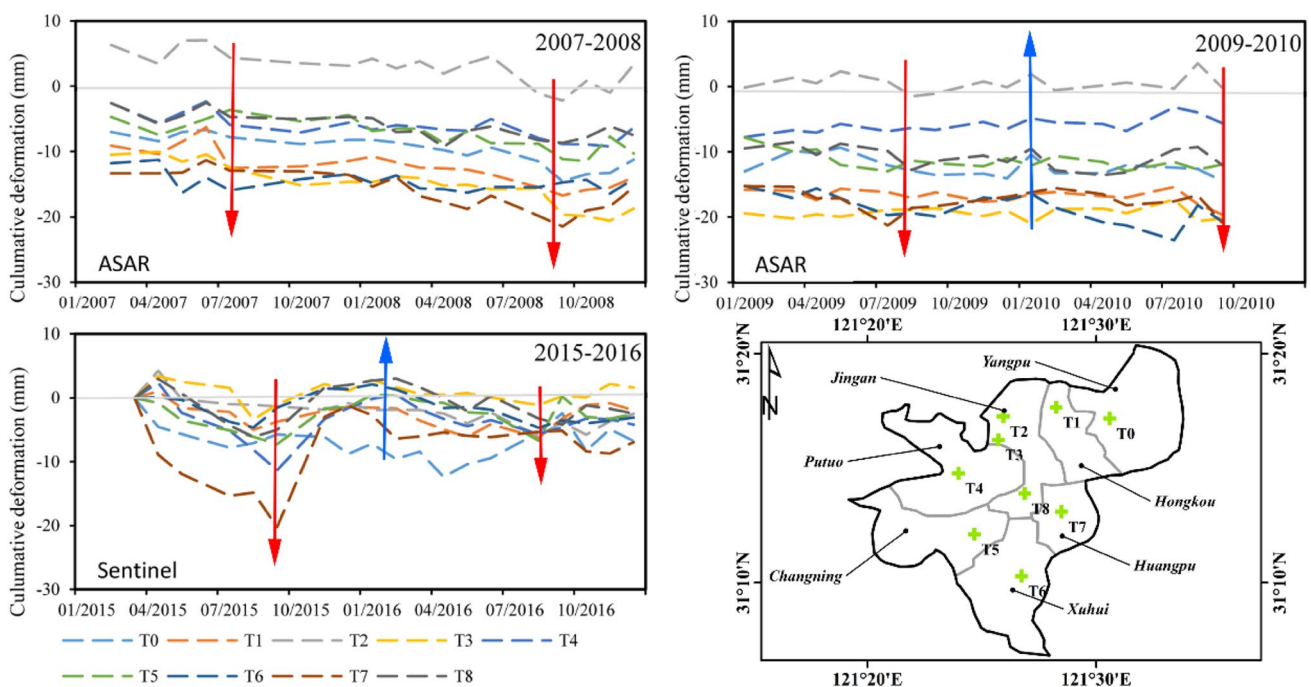
Fig. 5 The cumulative deformation curve in the urban area of Shanghai in 2007–2008, 2009–2010, and 2015–2016. The lower right map represents the distribution of the test points

rates were calculated by original data during 2004–2010 and 2015–2017, and compared with the deformation rates measured by SBAS algorithm (Table 3). The result (Fig. 6) showed that R^2 values ranged from 0.73 to 0.94 and standard deviation (σ) is less than 1.5 mm/year. It can be inferred that the SBAS result from two SAR data accurately measures the surface deformation of the city.

**Table 3** The deformation rates of each leveling point from leveling data and different SAR data

No.	ENVISAT ASAR		Sentinel-1A	
	InSAR	Leveling	InSAR	Leveling
1	− 0.42	0.05	− 0.3	− 0.09
2	− 0.64	− 0.34	− 0.84	− 0.95
3	− 0.87	− 0.98	− 0.46	− 0.57
4	0.12	− 0.31	0.3	− 0.43
5	− 0.04	0.02	− 0.06	− 0.04
6	− 0.27	− 0.85	0.15	− 0.09
7	− 0.57	− 0.79	0.21	0.13
8	− 0.29	0.37	0.95	0.28
9	− 2.16	− 2.26	− 0.05	− 3.48
10	–	–	0.66	0.14
11	–	–	− 5.97	− 5.45
12	–	–	− 0.61	− 0.63
13	–	–	− 0.19	− 0.38
14	–	–	− 1.76	− 1.30
15	–	–	0.57	0.48
16	–	–	− 0.22	− 0.68
17	–	–	− 0.17	− 0.21
8	–	–	− 0.44	− 0.30

Deformation process in different types of construction land

Six sub-areas of residential land, industrial land, and transportation land (two samples for each construction land type) were selected to obtain cumulative deformation curves to investigate the effects of different types of construction land on surface deformation. To ensure the consistency of the background conditions, the geological conditions of these areas were the same: the buried depth of the bedrock is 200–320 m, including marine landform and alluvial geomorphology, and the sediments are silty clay with a layer of fine sand (Compilation committee of Shanghai geological environment atlas 2002).
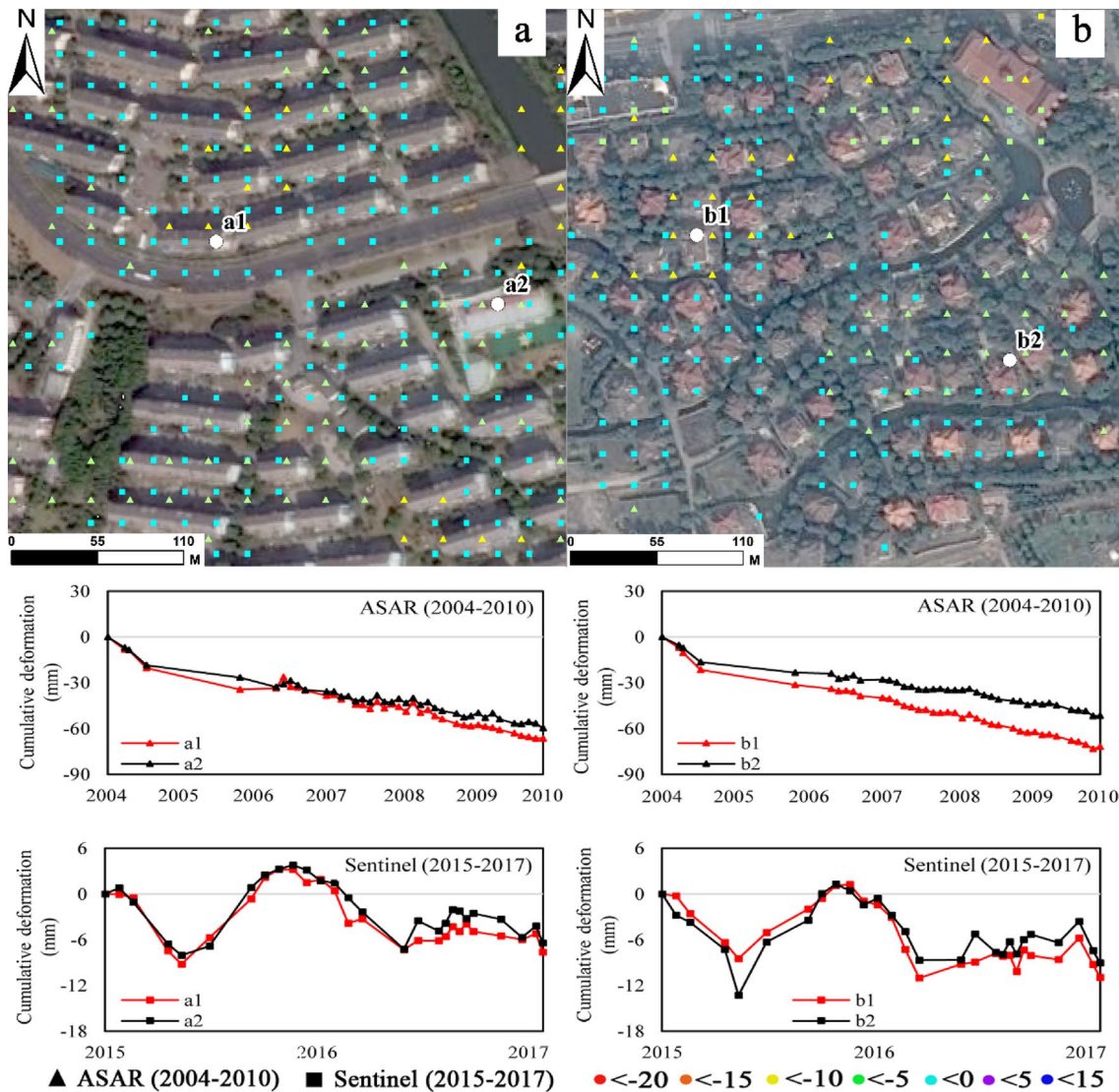
Deformation process of residential land

Shanghai has a relatively high population density with a large proportion of residential land, especially commercial housing and villa districts. The deformation rates in the commercial housing districts (Fig. 7a) were generally lower than those in the villa districts (the coherent points have different colors in the figure). The number of coherent points in villa districts is less than that in the commercial housing districts (Fig. 7b), due to the decoherence effect of the vegetation. A comparison of the cumulative deformation curves of the two districts showed that the deformation in the commercial housing districts was less than that in the villa district. The districts a and b were dominated by continuous surface subsidence, and the cumulative deformation was nearly 80 mm from 2004 to 2010. However, seasonal fluctuations appeared from 2015 to 2017. This phenomenon can be attributed to the processes of building construction. During the initial stage of the construction, the excavation of construction
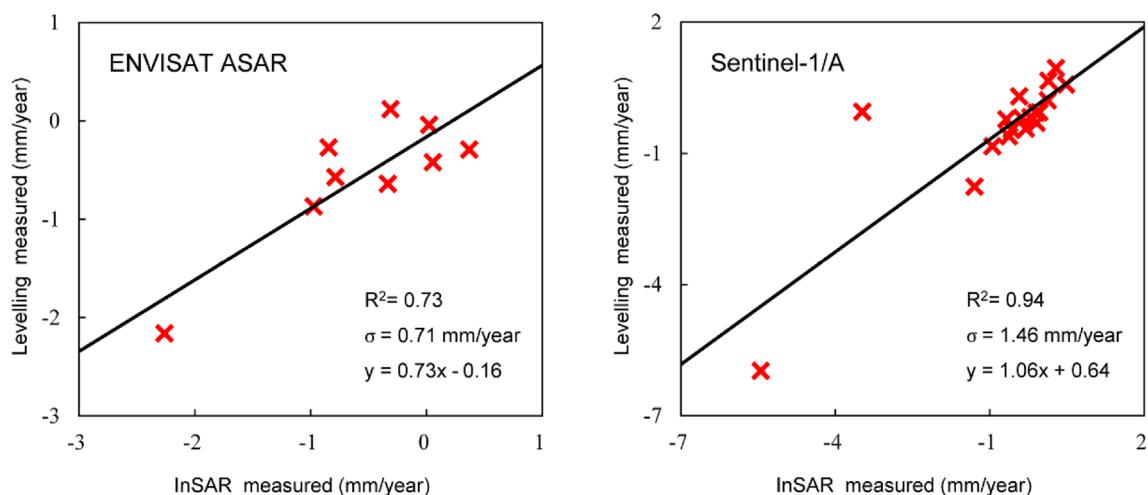
**Fig. 6** Comparison of deformation rates measured from leveling and InSAR

Fig. 7 The deformation rate distribution of two types of residential lands, and the four curves at the bottom display the cumulative deformation of commercial housing districts (a1, a2) and villa districts (b1, b2) during 2004–2010 and 2015–2017, respectively

foundations led to an increase in the compression of ground and the soil layer began to be compacted. This process corresponds to a large surface subsidence, and it will keep developing until the compaction threshold is reached. After that, surface subsidence tends to be stable and presents a seasonal fluctuation with the maximum subsidence occurring in September of each year, and then rebound until March of the next year (Fig. 7).

Deformation process of industrial land

During the urbanization process, the industrial land gradually shifted to the suburbs and accounting for large areas of land. Districts c and d are both industrial lands that were developed gradually since 2003; c1 and d1 are office

buildings, and c2 and d2 are plants and warehouses. The deformation rate of district c is less than that of district d, and the slopes of the subsidence of the office buildings in both areas are lower than that of the plants. This might be due to the large flow of workshop workers, cargo transportation and other mechanical transport, but office buildings do not have these issues. In 2004–2010, both districts c and d continued to subside with cumulative subsidence of up to 110–130 mm. In 2015–2017, fluctuating deformation occurred; the fluctuation in district d was greater, and the cumulative deformation was also the largest (nearly 40 mm), whereas district c has a relatively smooth deformation curve, and the cumulative deformation was less than 15 mm (Fig. 8).
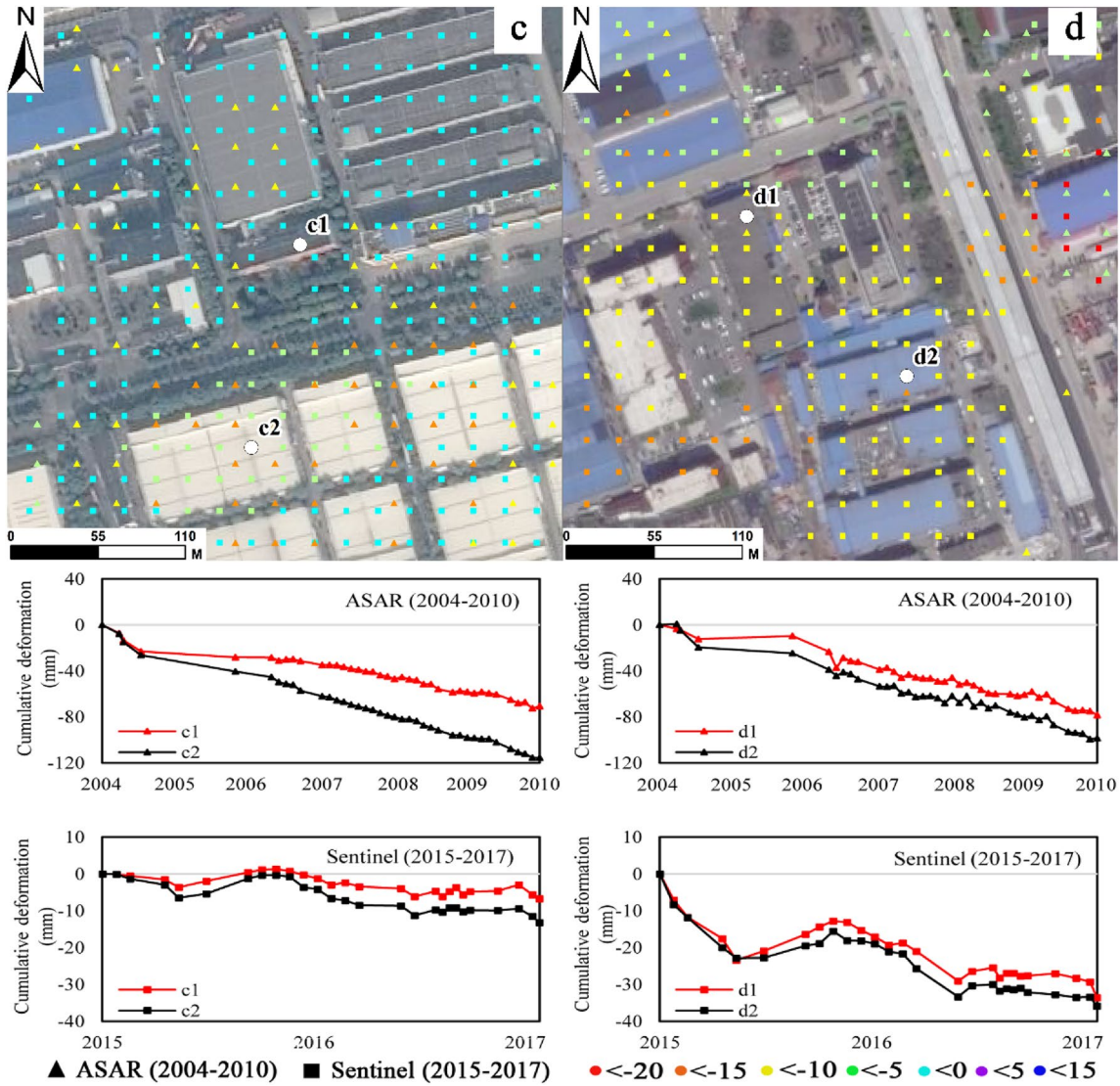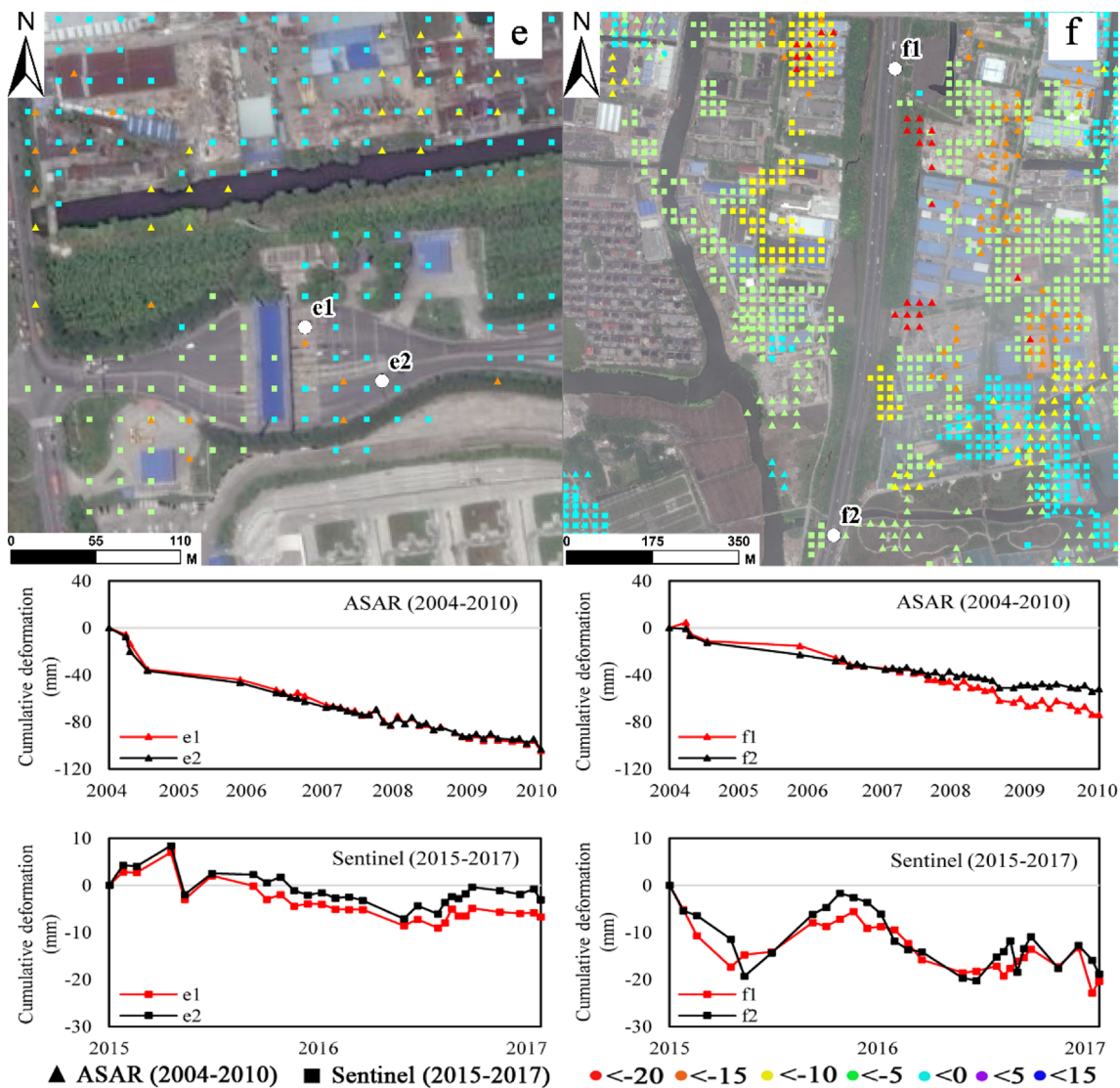
Fig. 8 The deformation rate distribution of industrial land, and the four curves at the bottom display the cumulative deformation of two types of buildings (c1, c2, d1, d2) in different industrial lands during 2004–2010 and 2015–2017, respectively

Deformation process of traffic land

Transportation continues to develop during the urbanization process and plays a role in connecting the main city to the suburbs. Most of the construction in these districts was for toll station (Fig. 9e) and inter-city highways (Fig. 9f). Construction started on the Caoan Toll Station (district e) in 2003, and it was put into use in 2004; district f is located in the Jiading–Jinshan section of the Shenyang–Haikou Expressway, which began construction in December 2003 and opened to traffic in November 2005.

The cumulative subsidence of district f was approximately 80 mm from 2004 to 2010, but that of district e reached 80 mm in 2008, and exceeded 110 mm in 2010 (Fig. 9). This indicates that the deformation subsidence degree of toll station

in the initial stage of construction is greater than highway. After many years of use, the deformation rate of district e significantly decreased, with cumulative deformation nearly 10 mm less than that in district f, and its curve is more stable in 2015–2017. There are also slight differences in surface deformation within the toll station. The subsidence at point e1, which is a toll collection area with a large vehicle flow, was slightly greater than that at point e2, which is a waiting area for vehicles.

Fig. 9 The deformation rate distribution of traffic land, and the four curves at the bottom display the cumulative deformation of toll station (e1, e2) and expressway (f1, f2) during 2004–2010 and 2015–2017, respectively

Conclusion

The ENVISAT ASAR and Sentinel-1A data from 2004 to 2017 were used to monitor the surface subsidence in Shanghai through long time series SBAS algorithm. The results showed that the surface subsidence in Shanghai has expanded from the urban area to the suburbs since 2004. The urban area gradually rebounded with a deformation rate decreasing from -14 mm/year to -8 mm/year and a decrease in the cumulative deformation. New areas of surface subsidence formed in the suburbs, mainly concentrated in the Fengxian District, which had deformation rates of -12 mm/year to -28 mm/year and a cumulative deformation as high as -43 mm.

Compared with the leveling data, R^2 is between 0.73 and 0.94, the standard deviation is less than 1.5 mm/year, which demonstrates that the surface deformation monitoring results based on the SBAS InSAR method are reliable. The results also showed seasonal fluctuations in the urban surface subsidence. The annual subsidence reached its maximum around July. Before this month it is the accumulation period of subsidence, after this month, the subsidence slows down and rebound occurs until around January of the following year, and a new period of subsidence accumulation begins.

Some constructions can cause regional subsidence by compacting the soil; this is consistent with Dong et al. (2014). Furthermore, the deformation characteristics vary in different construction project period. Under the same geological conditions, residential land had the lowest

deformation rate but large seasonal fluctuations, which mainly included the natural variations of surface subsidence, whereas industrial land had the highest deformation rate but minimal seasonal fluctuations. The transportation land had a higher deformation rate only during the initial stage of construction, the cumulative deformation decreased after construction was completed and this infrastructure was put into use, and the stability was second only to residential land. These descriptions of the deformation process of such long time series of various construction lands were unprecedented.

Urban surface deformation can be caused by multiple factors; therefore, it is necessary to integrate several data sources when analyzing its causes and characteristics. Additional surface-related information could be added to the existing InSAR algorithm, such as polarization interference SAR (PolInSAR), to fully use the properties of interference measurement changes with the polarization and to increase the recognition based on the scattering mechanism while obtaining the elevation phase. This would have significant applications for monitoring urban surface deformation and will be investigated further in the future.

References

Berardino P, Fornaro G, Lanari R, Sansosti E (2002) A new algorithm for surface deformation monitoring based on small baseline differential SAR interferograms. IEEE Trans Geosci Remote 40(11):2375–2383. https://doi.org/10.1109/TGRS.2002.803792

Cabral-Cano E, Dixon TH, Miralles-Wilhelm F, Diaz-Zlina O, Sanchez-Zamora O, Carande RE (2008) Space geodetic imaging of rapid ground subsidence in Mexico City. Geol Soc Am Bull 120(11–12):1556–1566. https://doi.org/10.1130/B26001.1

Chen BB, Gong HL, li XJ, lei KC, Zhao YQ, Li JW, Gu ZQ, Dang YA (2011) Spatial-temporal characteristics of land subsidence corresponding to dynamic groundwater funnel in Beijing Municipality, China. Chin Geogr Sci 21(6):753–764. https://doi.org/10.1007/s11769-011-0509-6

Chen J, Wu JC, Zhang LN, Zou JP, Liu GX, Zhang R, Yu B (2013) Deformation trend extraction based on multi-temporal InSAR in Shanghai. Remote Sens 5(4):1774–1786. https://doi.org/10.3390/rs5041774

Cigna F, Osmanoğlu B, Cabral-Cano E, Dixon TH, Ávila-Olivera JA, Garduño-Monroy VH, DeMets C, Wdowinski S (2012) Monitoring land subsidence and its induced geological hazard with Synthetic Aperture Radar Interferometry: a case study in Morelia, Mexico. Remote Sens Environ 117(1):146–161. https://doi.org/10.1016/j.rse.2011.09.005

Compilation committee of Shanghai geological environment atlas (2002) Shanghai geological environmental atlas. Geological Publishing House, Shanghai

Dang VK, Doubre C, Weber C, Gourmelen N, Masson F (2014) Recent land subsidence caused by the rapid urban development in the Hanoi urban region (Vietnam) using ALOS InSAR data. Nat Hazard Earth Sys 14(3):657–674. https://doi.org/10.5194/nhess-14-657-2014

Dong SC, Samsonov S, Yin HW, Ye SJ, Cao YR (2014) Time-series analysis of subsidence associated with rapid urbanization in Shanghai, China measured with SBAS InSAR method. Environ Earth Sci 72(3):677–691. https://doi.org/10.1007/s12665-013-2990-y

Fruneau B, Sarti F (2000) Detection of ground subsidence in the city of Paris using radar interferometry: Isolation of deformation from atmospheric artifacts using correlation. Geophys Res Lett 27(24):3981–3984. https://doi.org/10.1029/2000GL008489

Gabriel AK, Goldstein RM, Zebker HA (1989) Mapping small elevation changes over large areas: Differential radar interferometry. J Geophys Res Solid Earth 94(B7):9183–9191. https://doi.org/10.1029/JB094iB07p09183

Gatelli F, Guamieri AM, Parizzi F, Pasquali P, Prati C, Rocca F (1994) The Wave number Shift in SAR Interferometry. IEEE Trans Geosci Remote 32(4):855–865. https://doi.org/10.1109/36.298013

Ge DQ, Zhang L, Wang Y, Li M, Liu B (2014) Monitoring subsidence on Shanghai Metro line 10 during construction and operation using high-resolution InSAR. Shanghai Land Resour (4): 62–67. https://doi.org/10.3969/j.issn.2095-1329.2014.04.014 **(in Chinese)**

Gheorghe M, Armaş I (2016) Comparison of multi-temporal differential interferometry techniques applied to the measurement of Bucharest City Subsidence. Proc Environ Sci 32:221–229. https://doi.org/10.1016/j.proenv.2016.03.027

Guzzetti F, Manunta M, Ardizzone F, Pepe A, Cardinali M, Zeni G, Reichenbach P, Lanari R (2009) Analysis of ground deformation detected using the SBAS-DInSAR technique in Umbria, Central Italy. Pure Appl Geophys 166(8–9):1425–1459. https://doi.org/10.1007/s00024-009-0491-4

Hooper A (2008) A multi-temporal InSAR method incorporating both persistent scatterer and small baseline approaches. Geophys Res Lett 35(16):96–106. https://doi.org/10.1029/2008GL034654

Hooper A, Zebker H, Segall P, Kampes B (2004) A new method for measuring deformation on volcanoes and other natural terrains using InSAR persistent scatterers. Geophys Res Lett 31(23):1–5. https://doi.org/10.1029/2004GL021737

Jo MJ, Won JS, Kim SW, Jung HS (2010) A time-series SAR observation of surface deformation at the southern end of the San Andreas Fault Zone. Geosci J 14(3):277–287. https://doi.org/10.1007/s12303-010-0028-y

Lauknes TR, Dehls J, Larsen Y, Hogda KA, Weydahl DJ (2008) A comparison of SBAS and PS ERS InSAR for subsidence monitoring in Oslo, Norway. In: Fringe Workshop 25

Lin H, Chen FL, Zhao Q (2011) Land deformation monitoring using coherent target-neighbourhood networking method combined with polarimetric information: a case study of Shanghai, China. Int J Remote Sens 32(9):2395–2407. https://doi.org/10.1080/01431161003698328

Lubitz C, Motagh M, Wetzel HU, Kaufmann H (2013) Remarkable urban uplift in Staufen im Breisgau, Germany: observations from TerraSAR-X InSAR and Leveling from 2008 to 2011. Remote Sens 5(6):3082–3100. https://doi.org/10.3390/rs5063082

Massonnet D, Rossi M, Carmona C, Adragna F, Peltzer G, Feigl K, Rabaute T (1993) The displacement field of the Landers earthquake mapped by radar interferometry. Nature 364(6433):138–142. https://doi.org/10.1038/364138a0

Mouélic SL, Raucoules D, Carnec C, King C, Adragna F (2002) A ground uplift in the city of Paris (France) detected by satellite radar interferometry. Geophys Res Lett 29(17):1222–1224. https://doi.org/10.1029/2002GL015630

Nikos S, Ioannis P, Constantinos L, Paraskevas T, Anastasia K, Charalambos K (2016) Land subsidence rebound detected via multi-temporal InSAR and ground truth data in Kalochori and Sindos regions, Northern Greece. Eng Geol 209:175–186. https://doi.org/10.1016/j.enggeo.2016.05.017

Ogushi F, Shinohara T, Matsuoka M (2015) Surface displacement due to the 2014 North Nagano, Japan earthquake estimated from differential interferometry technique with ALOS-2 PALSAR-2 data. In: IEEE IGARSS, pp 3532–3536

Parcharidis I, Lagios E, Sakkas V, Raucoules D, Feurer D, Mouelic SL, King C, Carnec C, Novali F, Ferretti A (2006) Subsidence monitoring within the Athens Basin (Greece) using space radar interferometric techniques. Earth Planets Space 58(5):505–513. https://doi.org/10.1186/BF03351947

Pepe A, Zhao Q, Bonano M, Lu Z, Zhou Y (2015) The study of the deformation time evolution in coastal areas of Shanghai: a joint C/X-band SBAS-DInSAR analysis. In: IEEE IGARSS, pp 306–309

Pepe A, Bonano M, Zhao Q, Yang T, Wang H (2016) The use of C-/X-band time-gapped SAR data and geotechnical models for the study of Shanghai's ocean-reclaimed lands through the SBAS-DInSAR technique. Remote Sens 8:911. https://doi.org/10.3390/rs8110911

Perissin D, Wang Z, Lin H (2012) Shanghai subway tunnels and highways monitoring through Cosmo-SkyMed Persistent Scatterers. ISPRS J Photogramm Remote Sens 73:58–67. https://doi.org/10.1016/j.isprsjprs.2012.07.002

Pratesi F, Tapete D, Ventisette CD, Moretti S (2016) Mapping interactions between geology, subsurface resource exploitation and urban development in transforming cities using InSAR Persistent Scatterers: two decades of change in Florence, Italy. Appl Geogr 77:20–37. https://doi.org/10.1016/j.apgeog.2016.09.017

Sillerico E, Ezquerro P, Marchamalo M, Herrera G, Duro J, Martínez R (2015) Monitoring ground subsidence in urban environments: M-30 tunnels under Madrid City (Spain). Ing Invest 35(2):30–35. https://doi.org/10.15446/ing.investigv35n1.46614

Sowter A, Amat MB, Cigna F, Marsh S, Athab A, Alshammari L (2016) Mexico City land subsidence in 2014–2015 with Sentinel-1 IW TOPS: results using the Intermittent SBAS (ISBAS) technique. Int J Appl Earth Obs 52:230–242. https://doi.org/10.1016/j.jag.2016.06.015

Strozzi T, Wegmuller U (1999) Land subsidence in Mexico City mapped by ERS differential SAR interferometry. IEEE IGARSS 1940–1942. https://doi.org/10.1109/IGARSS.1999.774993

Sun G, Ranson KJ, Kharuk VI, Kovacs K (2003) Validation of surface height from shuttle radar topography mission using shuttle laser altimeter. Remote Sens Environ 88(4):401–411. https://doi.org/10.1016/j.rse.2003.09.001

Tapete D, Fanti R, Cecchi R, Petrangeli P, Casagli N (2012) Satellite radar interferometry for monitoring and early-stage warning of structural instability in archaeological sites. J Geophys Eng 9(4):10–25. https://doi.org/10.1088/1742-2132/9/4/S10

Wang ZY, Perissin D, Lin H (2011) Subway tunnels identification through Cosmo-SkyMed PSInSAR analysis in Shanghai. IEEE IGARSS 1267–1270. https://doi.org/10.1109/IGARSS.2011.6049430

Wright P, Stow R (1999) Detecting mining subsidence from space. Int J Remote Sens 20(6):1183–1188. https://doi.org/10.1080/014311699212939

Wu JC, Hu FM (2015) Ground subsidence monitoring of high speed roads by using PS-InSAR method. In: 2015 IEEE 5th APSAR, pp 853–858. https://doi.org/10.1109/APSAR.2015.7306337

Xiong FW, Zhu YW (2007) Land deformation monitoring by GPS in the Yangtze Delta and the measurements analysis. Chin J Geophys 50(6):1501–1514. https://doi.org/10.1002/cjg2.1170

Yan YJ, Doin MP, Lopez-Quiroz P, Tupin F, Fruneau B, Pinel V, Trouve E (2012) Mexico City subsidence measured by InSAR time series: joint analysis using PS and SBAS approaches. IEEE J-STARS 5(4):1312–1326. https://doi.org/10.1109/JSTARS.2012.2191146

Yang MS, Jiang YN, Liao MS, Wang HM (2013a) The analysis of the subsidence patterns in Lingang New City (Shanghai) Using high-resolution SAR images. Shanghai Land Resour 34(4):12–16. https://doi.org/10.3969/j.issn.2095-1329.2013.04.004 **(in Chinese)**

Yang Y, Pepe A, Manzo M, Bonano M, Liang DN, Lanari R (2013b) A simple solution to mitigate noise effects in time-redundant sequences of small baseline multi-look DInSAR interferograms. Remote Sens Lett 4(6):609–618. https://doi.org/10.1080/2150704X.2013.771826

Zebker HA, Villasenor J (1992) Decorrelation in interferometric radar echoes. IEEE Trans Geosci Remote 30(5):950–959. https://doi.org/10.1109/36.175330

Zebker HA, Rosen PA, Hensley S (1997) Atmospheric effects in interferometric synthetic aperture radar surface deformation and topographic maps. J Geophys Res Solid Earth 102(B4):7547–7563. https://doi.org/10.1029/96JB03804

Zhang WR, Duan ZL, Zeng ZQ, Shi HP (2003) Methods to control or arrest land subsidence and their economic benefit in Shanghai. J Tongji Univ 31(7):864–868 **(in Chinese)**

Zhao Q, Pepe A, Gao W, Lu Z, Bonano M, He ML, Wang J, Tang X (2015) A DInSAR investigation of the ground settlement time evolution of ocean-reclaimed lands in Shanghai. IEEE J-STARS 8(4):1763–1781. https://doi.org/10.1109/JSTARS.2015.2402168

Zyl JJV (2001) The Shuttle Radar Topography Mission (SRTM): a breakthrough in remote sensing of topography. Acta Astronaut 48(5–12):559–565. https://doi.org/10.1016/j.rse.2003.09.001